Creep rupture behavior of Grade 91 steel

Triratna Shrestha [a], Mehdi Basirat [b], Indrajit Charit [a,*], Gabriel P. Potirniche [b], Karl K. Rink [b]

[a] Department of Chemical and Materials Engineering, University of Idaho, Moscow, ID 83844, USA
[b] Department of Mechanical Engineering, University of Idaho, Moscow, ID 83844, USA

ABSTRACT

Grade 91 steel is considered a potential structural material for advanced nuclear reactors. The creep deformation behavior of Grade 91 steel was studied in the temperature range of 600–700 °C and at stresses of 35–350 MPa. The data were analyzed in terms of Monkman-Grant relation and Larson–Miller parameter. Creep damage tolerance factor and stress exponent were used to identify the cause of creep damage. The fracture surface morphology of the ruptured specimens was studied by scanning electron microscopy to elucidate the failure mechanisms. Fracture mechanism map for Grade 91 steel was developed based on the available material parameters and experimental observations.

© 2012 Elsevier B.V. All rights reserved.

1. Introduction

Since the introduction of Cr–Mo steels, they have been the material of choice for use in power generation plants. Ferritic–martensitic (F–M) steels with 9–12 wt% Cr were developed for fossil-fuel-fired power plants [1] during 1960s, and later used as boiler tube in the advanced gas-cooled reactors [2,3]. With optimization of alloy compositions, the creep rupture strength of F–M steels has increased significantly over the years [3]. For example, the composition of the earlier version of 9Cr–1Mo (T9) F–M steel was modified by addition of Nb and V to enhance the creep properties. Nb and V form fine, stable carbides and carbonitrides, resulting in excellent creep strength. These precipitates improve creep strength of the steel by resisting the movement of dislocations, delaying the plastic deformation by inhibiting grain boundary sliding, retaining finer grains during austenitization [4], and delaying the onset of tertiary creep stage [5]. Compared to austenitic steels, F–M steels tend to have better radiation swelling resistance [1], excellent thermo-physical properties, resistance to stress corrosion cracking in aqueous and chloride environments, and are less expensive [6].

With the vision to enhance the efficiency of power production and lower the emission of greenhouse gases, the new generation nuclear power plants are expected to operate at higher temperatures and radiation doses for longer service life (60 years and beyond). Hence, the materials used in these power plants are required to have superior creep properties. For example, Grade 91 steel is seen as a potential candidate material for reactor pressure vessel (RPV) application in Gen-IV Very High Temperature Reactor (VHTR). In addition to that, Grade 91 steel (also called modified 9Cr–1Mo steel) is being considered as wrapper material for Fast Breeder Reactors (FBR) [7]. Depending on the VHTR design, Prismatic Modular Reactor (PMR) or Pebble Bed Modular Reactor (PBMR), the operating temperature of the reactor pressure vessel (RPV) can vary between 300 °C and 650 °C. Furthermore, the RPV in the VHTR will be more than twice the size of a typical RPV in a Light Water Reactor (LWR) [8]. The nuclear power plant with a VHTR design is expected to produce electricity and hydrogen (a clean source of energy) at the same time.

RPV is considered an irreplaceable component of a nuclear power plant which dictates its useful service life. Hence, understanding creep rupture properties of Grade 91 steel is important to predict the long term mechanical integrity of the plant. Detailed study of creep deformation mechanisms in Grade 91 steel can be found in Shrestha et al. [9]. Even though there are a number of other studies involving creep deformation mechanisms of as-received Grade 91 steels [10–14], there are very few studies [12,15] in the area of their creep rupture behavior. Generally, it is not clear how creep deformation mechanism affects the creep rupture behavior which is dominated by the tertiary stage of creep. The creep rupture characteristics of Grade 91 steel have been analyzed by linking them with the identified creep deformation mechanism, and in terms of the Monkman–Grant relation, creep damage tolerance and Larson–Miller parameter. The data analysis was supported by fractography, which is used to identify the cause of creep rupture failure.

2. Experimental details

2.1. Material

The chemical composition of ASTM A387 Grade 91 CL2 steel (Grade 91) used in this study is shown in Table 1. The hot rolled Grade 91 plates were obtained from ArcelorMittal Plate LLC, in normalized and tempered condition (i.e., austenitized at 1040 °C for 240 min followed by air cooling, and tempered at 790 °C for 43 min). The as-received plates were 10.4 cm × 10.4 cm × 1.27 cm in size. Creep specimens with a gauge length of 2.54 cm and diameter of 0.635 cm were machined from the steel plates. At room temperature, the as-received Grade 91 steel exhibited yield strength of 533 MPa, ultimate tensile strength of 683 MPa and elongation to fracture of 19%.

2.2. Microstructural characterization

Optical microscopy was performed on both the as-received and creep tested specimens for characterization of the grain structure. Conventional metallographic procedures of cold mounting, grinding

Table 1
Chemical composition (in wt%) of Grade 91 steel.

Element	Nominal	Measured
Cr	8.00–9.50	8.55
Mo	0.85–1.05	0.88
V	0.18–0.25	0.21
Nb	0.06–0.10	0.08
C	0.08–0.12	0.10
Mn	0.30–0.60	0.51
Cu	0.4 (max.)	0.18
Si	0.20–0.50	0.32
N	0.03–0.07	0.035
Ni	0.40 (max.)	0.15
P	0.02 (max.)	0.012
S	0.01 (max.)	0.005
Ti	0.01 (max.)	0.002
Al	0.02 (max.)	0.007
Zr	0.01 (max.)	0.001
Fe	Balance	Balance

and polishing were followed to prepare the specimen surface to 0.5 µm finish before etching was carried out using Marble's reagent; a solution made of 50 ml distilled water, 50 ml hydrochloric acid and 10 g of copper sulfate. Subsequently, an Olympus light microscope was used to examine the metallographic specimens and an attached CCD camera was used to record the micrographs.

For detailed microstructural characterization, some metallographic samples were examined using a Zeiss Supra 35 field emission gun scanning electron microscope (FEG-SEM) operated at an accelerating voltage of 10–20 kV under both secondary and backscattered electron imaging modes. Energy dispersive spectroscopy (EDS) technique available in the SEM was used to estimate the relevant chemical compositions.

The ruptured samples were then sectioned from the gauge length of the specimen. For TEM study, the sectioned samples were mechanically polished down to ∼120 µm thickness, and then 3 mm diameter disks were punched out of the samples. Those disks were then jet polished in Fischione twin-jet polisher using a solution of 80 vol% methanol and 20 vol% nitric acid solution at a temperature of ∼ −40 °C. Dry ice bath was used to achieve low temperature. Philips CM200 and JEOL JEM-2010 TEM operated at an accelerating voltage of 200 kV were used to study in detail the grain and precipitate morphology of the material under both as-received and crept conditions. Hardness was measured using a Vickers microhardness tester; applied load was 500 gf (4.9 N) and the hold time was 15 s.

2.3. Creep testing

Creep tests were performed at different temperatures between 600 °C and 700 °C and stresses between 35 and 350 MPa using an Applied Test Systems (ATS) lever arm (20:1) creep tester. Though creep tests were intended for fracture, some tests in the lower stress regime were interrupted in the minimum creep stage due to time constrain.

3. Results and discussion

3.1. Microstructural characteristics of as-received material

The as-received Grade 91 steel had a tempered martensitic microstructure as shown in Fig. 1a. Precipitation hardening is one
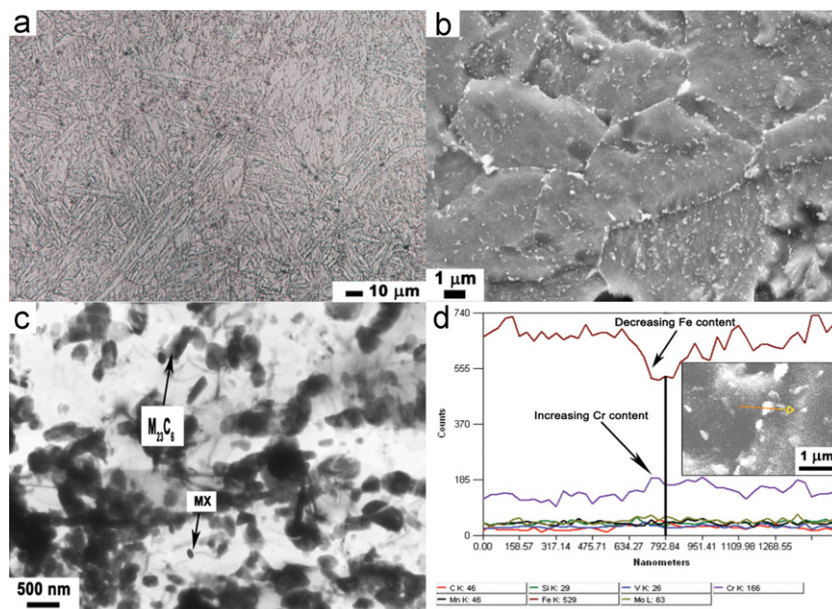

Fig. 1. Microstructure of Grade 91 steel: (a) optical micrograph showing the tempered martensitic structure, (b) a SEM micrograph showing the distribution of precipitates in the alloy, (c) a bright field TEM micrograph showing various particles, and (d) EDS line scan of $M_{23}C_6$ type particle.

of the main strengthening mechanisms in highly alloyed steels like Grade 91. Alloying elements, such as C, N, Nb, V, Cr and Mo, promote the formation of precipitates like Cr-rich $M_{23}C_6$, and Nb or V-rich MX particles, where M stands for metals, i.e., Cr, Mo, Nb or V, and X stands for C or N. The Cr-rich $M_{23}C_6$ precipitates are elongated rod-like or block-like particles, while Nb-rich and V-rich MX precipitates have nearly spherical shapes. The dimensions of the elongated rod-like and block-like Cr-rich precipitates were measured, and found to have an average length of 285 ± 80 nm and width of 121 ± 39 nm, which are similar to the ones reported in Grade 91 steel [5,13,16]. The average diameter of near-spherical MX-type precipitates was 37 ± 15 nm, similar to the values reported in Grade 91 steel [5,13,17]. These thermally stable fine precipitates enhance the long term creep resistance. A SEM micrograph in Fig. 1b shows the distribution of precipitates in the alloy. Coarser $M_{23}C_6$ type precipitates were located on the grain boundaries, lath boundaries and prior austenite grain boundaries, while finer MX type precipitates were located inside the grain. The TEM micrograph in Fig. 1c shows the various precipitates including $M_{23}C_6$ and MX types. Morphology of the $M_{23}C_6$ type precipitates was studied by EDS in SEM. The EDS line scan of these precipitates, as shown in Fig. 1d, revealed that the main constituents of $M_{23}C_6$ precipitate were Cr and plausibly Mo.

3.2. Creep properties

During the primary creep, the creep rate decreases with increasing strain due to work hardening via dislocation multiplication and interactions. In the secondary stage, creep rate is stabilized as the work hardening effect is counter balanced by the dislocation annihilation and rearrangement. Finally, the creep rate accelerates as cavities start growing leading to the tertiary stage. Most creep curves obtained in this study consisted of two distinct regimes: primary and tertiary, and a minimum creep rate regime in the transition. Fig. 2a shows the effect of applied stress on the creep rate at a temperature of 600 °C. Minimum creep rates increased but rupture time decreased with increasing applied stress. Fig. 2b shows the effect of test temperature on creep rate at a stress of 100 MPa. The minimum creep rates increased but rupture time decreases with increasing temperature. Table 2 lists the summary of creep rupture data. All the data were obtained from power law creep regime.

The total creep rupture life is related to the duration of primary and secondary creep stage by the following relationship:

$$\frac{t_R^\gamma}{t_{ts}} = C, \tag{1}$$

where t_{ts} is the time to reach tertiary creep stage, t_R the rupture time, C and γ are constants. When t_{ts} data were plotted against t_R data in a double logarithmic scale, all the data fall on a straight

line whose slope is the value of constant γ (~ 1.12) as shown in Fig. 3a. It is noted that the relation between the time to reach tertiary creep stage and the rupture time is independent of temperature. Creep rupture data for various temperatures are presented as stress versus rupture time as shown in Fig. 3b. Here straight lines were obtained for each temperature. No change in the slope was noted for any particular temperature implying that the creep damage mechanism remained the same. Nevertheless, the knowledge of such microstructural instabilities is important since they could lead to significant errors in extrapolation of the data to longer time [18].

3.2.1. Creep deformation mechanism

Here creep deformation mechanism in the higher stress regime was analyzed based on the minimum creep rates using the Bird–Mukherjee–Dorn (BMD) equation [19]

$$\frac{\dot{\varepsilon}_m kT}{DEb} = A\left(\frac{\sigma}{E}\right)^n \left(\frac{b}{d}\right)^p, \tag{2}$$

where A is a constant, $\dot{\varepsilon}_m$ the minimum creep rate, E the modulus of elasticity, b the Burgers vector, k the Boltzmann constant, T the absolute temperature, σ the applied stress, d the grain diameter, p the inverse grain size exponent, n the stress exponent, and D the diffusivity which is described by the following relation:

$$D = D_o \exp\left(\frac{-Q}{RT}\right), \tag{3}$$

where D_o is the frequency factor, Q the appropriate activation energy, and R the universal gas constant. However, for particle hardened alloys like Grade 91 steel, the BMD equation tends to result in higher activation energy and stress exponent [9]. In this study, the apparent stress exponents of 11 and 9, and high

Table 2
Summary of creep rupture data.

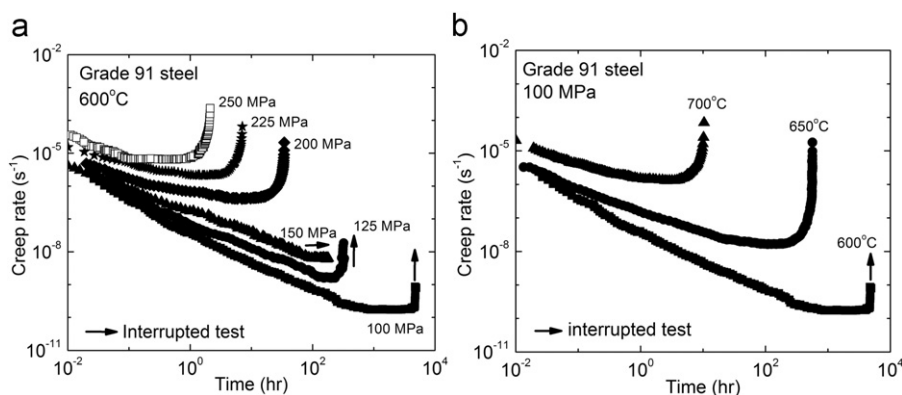| Sample	Temp. (°C)	Stress (MPa)	Fracture elongation (%)	Reduction in area (%)	True fracture strain
1	600	200	21	87	2
2	600	225	21	87	2
3	600	250	19	85	1.9
4	600	275	24	85	1.9
5	600	310	26	85	1.9
6	650	100	24	85	1.9
7	650	125	21	90	2.3
8	650	150	30	92	2.5
9	650	200	16	90	2.2
10	700	80	20	94	2.9
11	700	100	23	93	2.7
12	700	200	27	97	3.4

Fig. 2. (a) The variation of creep rates as a function of stress at 600 °C and (b) the variation of creep rates with temperature at 100 MPa.
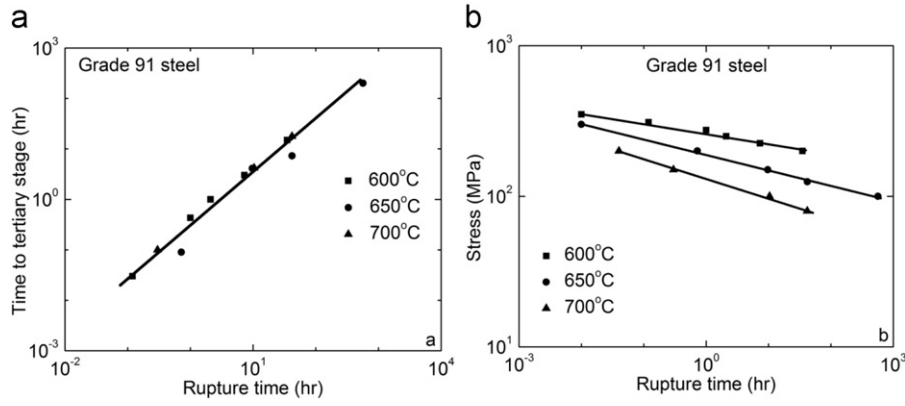
Fig. 3. (a) Relation between the creep rupture life and the time to get to tertiary creep stage and (b) stress and temperature dependency of creep rupture life.
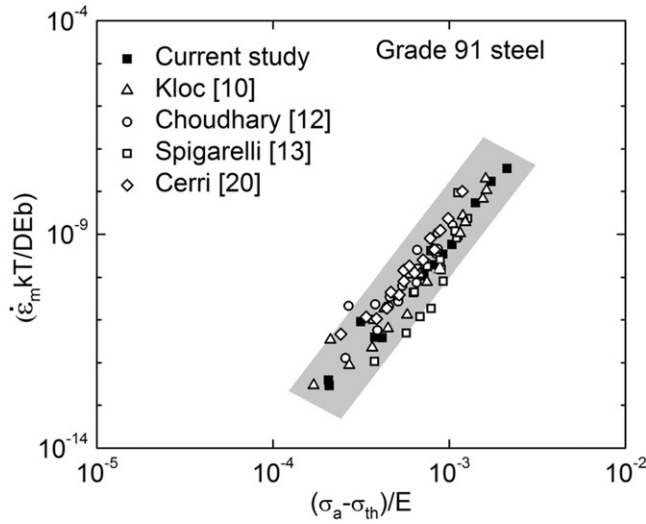

Fig. 4. Modified BMD plot involving normalized creep data for various Grade 91 steels.

activation energy of 510 kJ/mol were obtained. The BMD equation was modified to incorporate the threshold stress (σ_{th}). The threshold stress compensated constitutive equation can then be described by

$$\frac{\dot{\varepsilon}_m kT}{DEb} = A\left(\frac{\sigma-\sigma_{th}}{E}\right)^n \left(\frac{b}{d}\right)^p, \qquad (4)$$

where ($\sigma - \sigma_{th}$) is the effective stress. Even though the above equations are used to describe the creep deformation behavior in the minimum creep regime, they do provide insights into the failure mechanisms that occur during the tertiary stage of creep. After incorporating the threshold stress, the rate controlling creep deformation mechanism in the high stress regime was identified as climb of edge dislocations, the high apparent stress exponents of 11 and 9 were reduced to 5 (true stress exponent), and the creep activation energy was reduced from 510 kJ/mol to 225 kJ/mol, which is close to the activation energy of lattice self-diffusion in α-iron. Fig. 4 shows the normalized ($\dot{\varepsilon}_m kT/DEb$) data plotted against modulus-compensated effective stress ($\sigma - \sigma_{th}/E$). Here compilation of data from other studies [10,12,13,20] were superimposed on the ($\dot{\varepsilon}_m kT/DEb$) versus ($\sigma - \sigma_{th}/E$) plot. Based on the plot shown in Fig. 4, the constant A was calculated to be 7.3×10^5. Though most of the compiled and present study data are within a band, some data are sparse.

3.2.2. Microstructural characteristics of crept specimen

The solid solution strengthening, fine substructure, dense dislocation network and precipitates increase the creep resistance of Grade 91 steel. These strengthening mechanisms deteriorate over time during creep, and the material loses its inherent creep rupture strength. The microstructural studies of specimen crept at 650 °C and 200 MPa, as shown in Fig. 5a, showed decrease in the dislocation and precipitate density. Creep strength is reduced in precipitate-free matrix as there are no obstacles for the movement of dislocations. Apart from deterioration of above mentioned strengthening mechanisms, precipitation of Laves phase (Fe_2Mo) weakens the creep strength by removing Mo from solid solution. The creep strength of an alloy depends on its ability to withstand temperature and stress for prolonged period of time and maintain its as-received microstructure. Degradation of creep strength has been correlated with changes in microstructure [17,21–23]. Polygonized microstructure can be seen in the gauge section of crept specimen, as shown in Fig. 5a, but in contrast, martensitic lath structure can still be seen in the grip section, as shown in Fig. 5b, which does not experience stress, just the temperature. The TEM studies revealed a decrease in the dislocation and precipitate density, and an increase in the subgrain size. Panait et al. [17] assert that the growth of subgrains during creep contributes most to the decrease in long-term creep resistance. According to Qin et al. [24] the evolution of subgrain size is given by the following relation:

$$\log \lambda = \log \lambda_s + \log\left(\frac{\lambda_0}{\lambda_s}\right)\exp\left(\frac{-\varepsilon}{k_w}\right), \qquad (5)$$

where λ is the subgrain size, $\lambda_s = 10Gb/\sigma$ is the subgrain size in the steady state regime, λ_o is the subgrain size in as-received condition, ε is the creep strain, $k_w \approx 0.12$ is a growth constant, G is the shear modulus, b is the Burgers vector and σ is the applied stress. The mean subgrain size in 12Cr1MoV, P91 and P92 steels was 0.35–0.42 μm [25]. In P92 steel at 600 °C and 160 MPa, the subgrain size increases from 700 nm at 1.8% strain to 1400 nm at 22.8% strain [11]. In our study, the average size of subgrains in the as-received condition was 0.15–0.4 μm. In a test done at 650 °C and 200 MPa, the subgrain size in grip and gauge section of creep specimen was 0.5 μm and 0.7 μm, respectively.

3.3. Fractography

The creep specimens ruptured with external necking and the associated percentage reduction in area, in many cases, was ~90% as shown in Table 2. The reduction in area percent increased with increase in temperature. In addition to the microstructural instability, the reduction in load bearing cross-section is a result
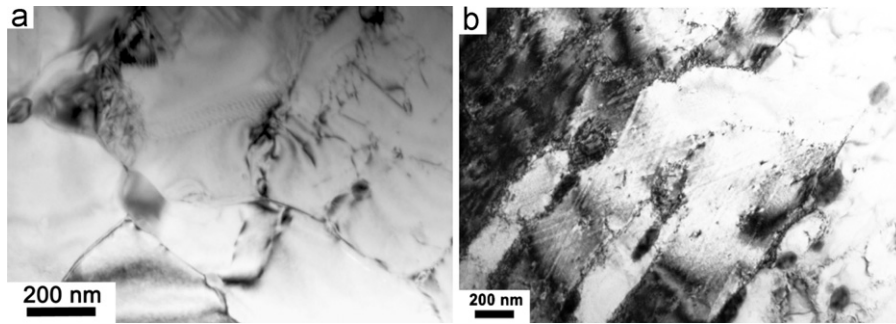
Fig. 5. Bright field TEM micrographs of a specimen crept at 200 MPa and 650 °C: (a) microstructure of the gauge section showing polygonized structure and (b) martensitic lath structure in grip section, which does not experience stress.
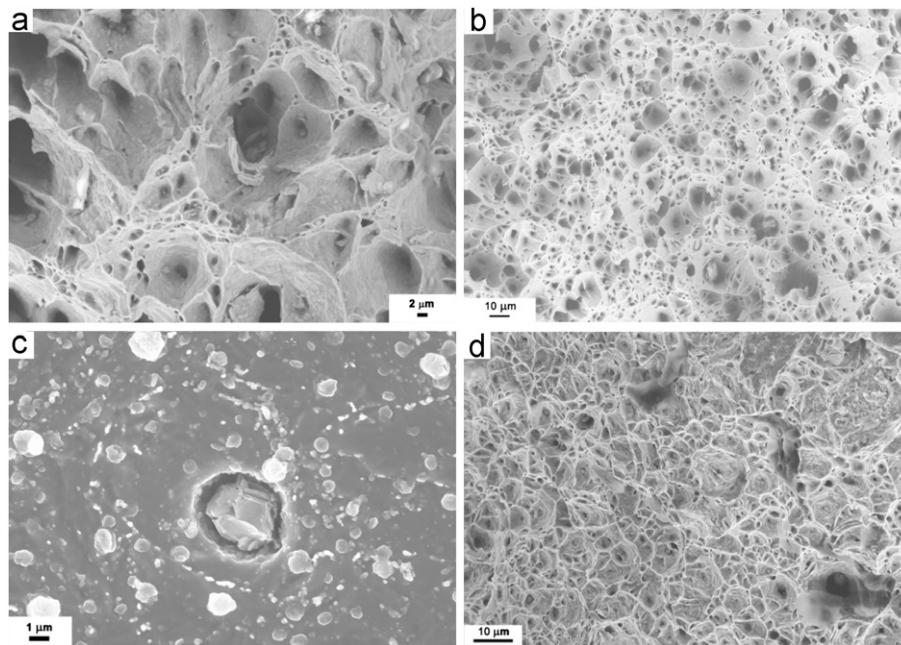

Fig. 6. (a) Dimpled fracture surface in specimen crept at 100 MPa and 650 °C, (b) ductile dimple fracture in specimen crept at 80 MPa and 700 °C, (c) cavity formation around a particle (600 °C and 200 MPa), and (d) dimpled fracture surface in specimen crept at 200 MPa and 650 °C.

of Fe–Cr oxides, which corresponds to ~2% decrease in load-bearing cross-section for a Grade 91 steel crept at 650 °C and 155 MPa for 31 h [15]. The reduction in load bearing cross-section can be significant for specimens crept for extended period of time. However, the significance of internal necking through the microstructural degradation, cavity formation, growth and coalescence must be taken into account to understand the final failure mechanism. It is important to note that none of the specimens failed through necking down to a point implying that internal damage processes had a significant bearing on their failure. Generally, cavities form throughout the creep deformation; however, in the tertiary stage nucleation and growth of cavities take place at an accelerated pace.

SEM study of fracture surface of the crept specimens revealed dominant dimple features, as shown in Fig. 6. These features are characteristic of transgranular mode of fracture. Similar fracture morphology was also reported by Yurechko et al. [15] in Grade 91 steel. Fig. 6a shows the fracture surface of a specimen crept at 650 °C and 100 MPa, while Fig. 6b shows the fracture surface of a specimen crept at 700 °C and 80 MPa. Transgranular fracture mode was also observed in a sample crept at 700 °C and 200 MPa, but the number density of cavities was lower while the average size was larger. For creep-enhanced diffusive cavity

growth, increasing stress leads to greater cavity growth rates and coalescence resulting in a smaller number density and larger dimple size.

While precipitates increase the creep strength of materials by impeding the dislocation motion, they act as the stress concentration sites for cavity nucleation during creep deformation. Creep damage in general is due to the combined effect of cavity nucleation, growth and coalescence. The cavities act as a stress raiser where the localized stress exceeds the applied stress. Because of some ductility of the steel, the stress concentration site undergoes plastic deformation. Ultimately, excessive plastic strain at the particle–matrix interface will lead to decohesion. That phenomenon can be further exacerbated via grain boundary sliding if the particle is located at the grain boundary [26]. Fig. 6c shows the cavity formation around a carbide precipitate in a specimen crept at 200 MPa and 600 °C. Precipitates were seen in the dimpled fracture surface, which suggests that the carbides aided in the cavity formation.

SEM was used to do the cavitation study on the necked area of the fractured specimens. Fig. 7a shows a low magnification SEM image of the cavities present in the necked region of a specimen crept at 200 MPa and 700 °C, which was taken ~5 mm away from the fractured surface. From the SEM image in Fig. 7a and also
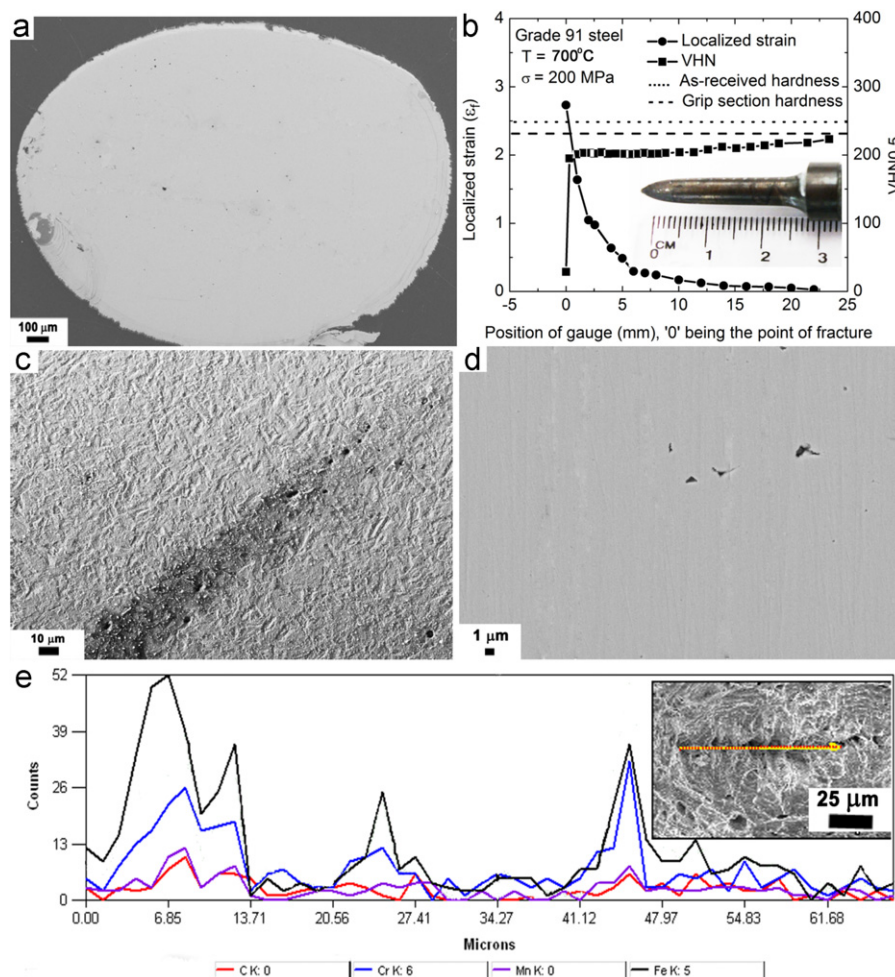
Fig. 7. (a) Necked area of a creep ruptured specimen (700 °C and 200 MPa), (b) variation of true local strain and microhardness with position in a specimen fractured at 700 °C and 200 MPa, (c) nucleation of voids along a straight line in a specimen crept at 650 °C and 100 MPa, (d) wedge cracks seen in a specimen crept at 150 MPa and 650 °C, and (e) EDS line scan along grain boundary.

images of higher magnification, no significant cavitation was observed. At this region on the gauge section, the local reduction in area was only ~0.5. The percentage reduction in area and the corresponding true fracture strain are listed in Table 2. The extent of cavitation depends on the amount of local strain. Fig. 7b shows the variation of true local strain and Vickers microhardness with the position on the gauge length of the aforementioned crept specimen. The fracture point is indicated as '0' which has the highest true strain of 3.4. True local strain decreases as we move away from the fracture point. The region where the creep damage is concentrated and has high true strain undergoes true tertiary stage, while other parts on the gauge showing little true strain have not reached the tertiary creep stage. However, the gauge section undergoing tertiary creep is so dominant that it becomes responsible to the final failure of the specimen. Further evidence of that is noted in the microhardness data shown in Fig. 7b. The microhardness increased as we moved away from the point of fracture. The point of fracture showed drastic decrease in hardness of 29VHN compared to 231VHN at the grip section and 248VHN of the as-received material. The hardness decreased with increasing number of cavities.

For a creep test performed at 100 MPa and 650 °C, localized creep cavitation at ~5 mm away from fracture tip can be seen in Fig. 7c. These creep cavities are found to be aligned along a more or less straight path and are round or elliptical shaped (r-type crack). This is likely due to the propensity of cavities forming on

the straighter lath boundaries. Growth of incipient r-type crack is controlled by diffusion but as the cavity size increases they grow by power law creep, and in transition they grow as a coupled effect of diffusion and power law creep [27]. Another example of damage initiation is noted in Fig. 7d where it shows a triple-point crack, ~7 mm away from the fracture tip, in a creep specimen tested at 150 MPa and 650 °C. These types of cracks are known as wedge shaped cracks (w-type cracks). Because of tensile stress, the grain boundaries which have precipitates and are normal to the applied stress are activated and the cavity grows as a result of the sliding of grains. In this study, all specimens failed predominantly in transgranular mode, but there was limited evidence of wedge cracks. The EDS line scan of fracture surface along the grain boundary shows the presence of Cr containing precipitate, as shown in Fig. 7e.

Apart from the $M_{23}C_6$ and MX type carbides, the manganese sulfide particles may also act as cavity nucleation site in Grade 91 steel. With the help of scanning auger microprobe, Hippsley [28] reported observing segregation of sulfur along the crack tip. Choudhary et al. [29] reported observing wedge crack in plain 9Cr–1Mo steel which is due to the split in the lath boundaries. The split in the lath boundaries was promoted by the presence of silicon and phosphorous. Grade 91 steel has 0.02 wt% phosphorus, which is higher than 0.007 wt% in 9Cr–1Mo steel. The higher phosphorous content makes the Grade 91 steel susceptible to phosphorous embrittlement [7].

3.4. Creep rupture data analysis and life prediction

The relationship between minimum creep rate and rupture life is given by the Monkman–Grant equation [30]

$$\dot{\varepsilon}_m{}^m t_R = K_1, \qquad (6)$$

where $\dot{\varepsilon}_m$ is the minimum creep rate, t_R the rupture time, m and K_1 are constants. The value of $K_1 = 0.04$ was obtained from straight line fit of the logarithmic relation deduced from Eq. (6). Nabarro [31] noted that for better prediction of creep rupture life m needs to be less than 1. In this study, m was calculated to be ~ 0.9. Thus, using the above relationship creep rupture life was predicted based on the experimentally determined minimum creep rate. From Eq. (6) and creep deformation plot reported by Shrestha et al. [9], the stresses for creep rupture life of 10^5 h in Grade 91 steel are predicted to be 87 MPa and 54 MPa at 600 °C and 650 °C, respectively. The creep life prediction for 600 °C is similar to one reported by Srinivasan et al. [32] using various creep life prediction methods.

Monkman and Grant [30] and Evans [33] found that the value of K_1 was 0.04 for ferritic steel and 0.08 for austenitic steel, and predicted that the K_1 to be less than n^{-1}, meaning that the data from Newtonian viscous creep regime were not included. Shrestha et al. [9] have calculated the stress exponent of ~ 10 in the higher stress regime before the incorporation of threshold stress in BMD equation. Stress exponent higher than 9 is common in engineering alloys like Grade 91 steel. The inverse of the calculated stress exponent (n) was ~ 0.1. The fit in Fig. 8a resulted in K_1 to be 0.04. For a material to fail by complete necking, K_1 has to be equal to n^{-1} [33]. Thus, necking is not the dominant fracture mode in the creep rupture tests reported in this study.

With regards to engineering alloys like Grade 91 steel, Dobes and Milicka [34] modified the aforementioned Monkman–Grant relation to obtain better correlation of the rupture time with the minimum creep rate by an equation

$$\dot{\varepsilon}_m{}^{m'} \frac{t_R}{\varepsilon_f} = K_2, \qquad (7)$$

where ε_f is the strain at fracture (based on elongation to fracture), K_2 and m′ are constants. The value of $K_2 = 0.26$ was found from the fitting of logarithmic plot deduced from Eq. (7), as shown in Fig. 8b. Eq. (7) was used to calculate the creep damage tolerance factor, λ. For m′=1, λ is given by inverse of K_2 [35,36]. The creep damage tolerance factor is used as a measure to identify the creep rupture mode whose value for engineering alloys range from 1 to 20 [36]. For $\lambda=1$, materials have low creep strain, and brittle fracture mode is detected as they fracture without any significant plastic deformation, while large values indicate that the material can withstand strain concentration without local cracking and the

fracture is ductile [31,36]. Ashby and Dyson [36] suggested that λ in the range of 1.5 and 2.5 indicates that damage is due to the cavity growth resulting from combined effect of power law and diffusion creep. Incipient cavities grow by diffusion, but power law creep takes over as they become larger [27]. For tests performed in higher stress regime (125–275 MPa) and at temperatures of 550 °C, 575 °C and 600 °C, Choudhary and Samuel [12] reported observing high λ close to 5. High λ value was attributed to the absence of intergranular cracks, absence of wedge shaped cracks, and the microstructural degradation like precipitate coarsening. Dominant creep damage mechanism is necking for λ higher than 2.5 [36], while coarsening of precipitates and subgrains, and decrease in dislocation density are the dominant creep damage mechanism when λ is 5 or higher [36,37]. Creep damage tolerance λ of 1.5 was observed in MA957, an yttrium bearing oxide dispersion strengthened (ODS) ferritic alloy, which fractured with little evidence of neck formation [38]. In this study, creep damage tolerance factor of ~ 4 was observed. The λ of ~ 4 indicates that the creep damage is due to the cavity growth resulting from combined effect of power law and diffusion creep, necking and microstructural degradation. Sometimes precipitates act as cavity nucleation sites, that is why some wedge type cracks and intergranular fracture mode was observed in this study, as shown in Fig. 7d. The reduction in area as indicated in Table 2 was similar to the one reported in [39]. Creep deformation mechanism of Grade 91 steel in high stress regime is controlled by power law creep [9,13,14]. Coarsening of precipitates and subgrains which were observed in Grade 91 steel [17,21–23] can decrease the creep strength as they become less effective in disrupting the movement of mobile dislocations [9,40]. The creep damage tolerance is expected to be ~ 5 when coarsening of precipitates and subgrains are the dominant failure mechanism [36]. But the values of K_1 (~ 0.04), which is less than n^{-1} (~ 0.1), and the creep damage tolerance higher than 2.5 indicate that the dominant failure mechanism in Grade 91 steel is microstructural degradation with limited contribution from necking, and void growth. This is illustrated in diagnostic diagram for creep failure as shown in Fig. 9 [36]. The figure shows that all the creep fracture data reported in this study fell on the microstructural degradation domain, except for the test done at 700 °C and 200 MPa. Data from aforementioned test fell on the loss of section and necking domain. The same test showed significant necking, and had the highest true fracture strain of 3.4 as listed in Table 2. Note that the Ashby's diagnostic diagram for creep failure map uses the apparent stress exponent (as obtained from Norton's law), not the true stress exponent (as obtained from modified BMD equation). Details of constructing such maps are given in the work of Ashby and Dyson [36]. Moreover, the creep rupture data of precipitation strengthened
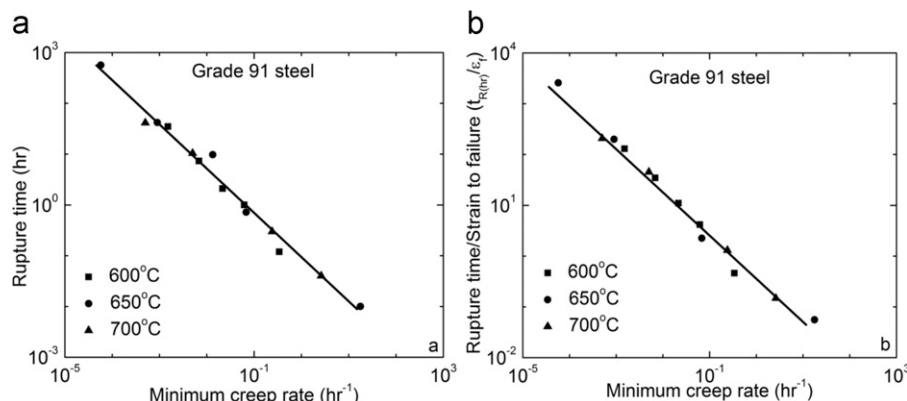

Fig. 8. (a) Monkman–Grant relation, and (b) modified Monkman–Grant relation.
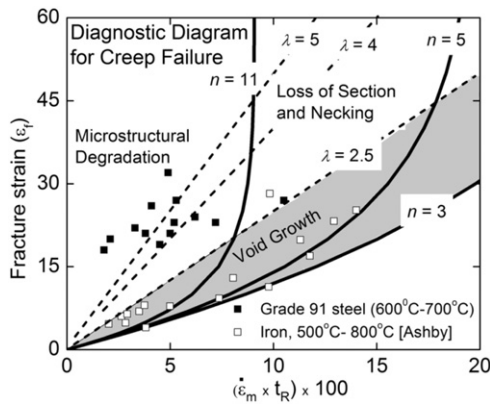
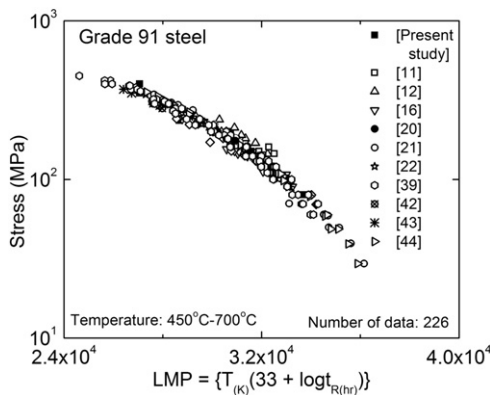**Fig. 9.** A diagnostic diagram for creep failure of Grade 91 steel and iron.

Fig. 10. Larson–Miller parameter plot of Grade 91 steel [42–44].

Table 3
Creep life prediction of Grade 91 steel by LMP.

Temp. (°C)	Rupture life (h)	Predicted allowable stress (MPa)
500	10^5	241
525	10^5	199
550	10^5	161
575	10^5	123
600	10^5	91
625	10^5	68
650	10^5	47
675	10^5	33
700	10^5	21

Fig. 11. Fracture mechanism map of Grade 91 steel.

Grade 91 steel were compared with that of iron. The dominant creep fracture mechanism in iron is void growth, while Grade 91 steel with more complex microstructure (as show in Fig. 1) exhibits microstructural degradation as the most dominant creep fracture mechanism.

Another way of presenting creep rupture data for creep life prediction is through Larson–Miller parameter (LMP). LMP can be expressed in terms of rupture time and temperature as

$$LMP = T(\log t_R + C),\qquad(8)$$

where T is the temperature (K), t_R the rupture time (h), and C the Larson–Miller constant, typically taken as 33. LMP values of Grade 91 steel decrease with increased stress, and the data obtained in the present study remain within the ambit of the data band obtained from other studies, as shown in Fig. 10. A best fit polynomial equation for stress versus LMP plot (Fig. 10) was used to predict the creep life of Grade 91 steel in the 500–700 °C temperature range. Table 3 lists the creep life prediction of Grade 91 steel. Thus, predicted creep life for 10^5 h rupture life is similar to the ones predicted by Srinivasan et al. [32] and Wilshire and Scharning [41] using various creep life prediction techniques. Klueh noted that the LMP plots for creep rupture tests of various steel types showed greater data scatter at low temperatures and high stresses than for the high temperatures and low stresses [3]. Even though the Monkman–Grant relation and LMP can be used to predict rupture life, it does not provide us with insights of the creep failure mechanisms. These approaches are empirically based, so their use may not lead to the precise estimation of the creep rupture life. Detailed study of temperature dependence on creep life prediction can be found in Srinivasan et al. [32] and Wilshire and Scharning [41].

3.5. Fracture mechanism map of Grade 91 steel

Fracture mechanism map of Grade 91 steel was constructed in two-dimensional space of normalized stress and homologous temperature using relevant constitutive equations, tensile data, and fracture data from current study and literature [12,15]. Five fracture mechanisms have been identified as shown in Fig. 11. Since this study is mainly focused on the creep rupture behavior of Grade 91 steel, the low temperature cleavage fracture is not included in this map. Each fracture regime was obtained from relevant models and supported by the fractographic observation. Material parameters obtained from reference [47] were for F82H F–M steel similar to Grade 91 steel. The major alloying elements in F82H steel are 8 wt% Cr and 2 wt% W, instead of 9 wt% Cr and 1 wt% Mo. Due to limited fractographic observations, variation in test condition, variation in grain size, lack of material parameters, and because of the fact that some of the models are not well-established, the map presented here is the best approximate mechanistic representation of the fracture behavior of Grade 91 steel under different test conditions. Material parameters used for construction of this fracture mechanism map are listed in Table 4.

Fracture at the ideal strength is defined as [18]

$$\sigma_{ideal} \approx \frac{E(T)}{10},\qquad(9)$$

where $E(T)$ is the temperature dependent modulus of elasticity. The dynamic fracture is the region in between the ideal strength fracture and ductile fracture regimes. Dynamic fracture is observed in a material when it is loaded at high strain rates. Grade 91 steel fractures by plastic deformation resulting in necking, which is the localized reduction in diameter of the test specimen. Necking introduces triaxiality of stress in the radial, transverse and longitudinal directions. The average true stress increases with decreasing cross-sectional area. Ductile fracture is

Table 4
Material parameters used in this study.

Parameter	Value	Reference
T_m (K)	1800	[46]
b (nm)	0.248	[46]
Ω (m^3)	1.38×10^{-29}	[46]
E_o (GPa)	223	
$\frac{T_m d\mu}{\mu_o dT}$	-1.09	[48]
Q_{gb} (kJ/mol)	150	[46]
A	7.3×10^5	
B	0.05	
a (μm)	1	[46]
δD_o^{gb}	1.0×10^{-13}	[46]
v	0.3	

observed in materials that have large strains in the range of 10–100% [45]. The ductile fracture domain was determined from the data obtained from tensile test performed at various temperatures. The higher domain of ductile fracture is the true fracture stress [46]

$$\sigma_{FS} = \sigma_{TTS}(1 + \varepsilon_f - \varepsilon_u), \tag{10}$$

where ε_f is the true fracture strain, ε_u the strain at uniform elongation, σ_{FS} the true fracture stress, and σ_{TTS} the true ultimate tensile stress given by [46]

$$\sigma_{TTS} = \sigma_{TS}\exp(\varepsilon_u), \tag{11}$$

where σ_{TS} is the engineering ultimate tensile stress. The true tensile stress is the lower domain of the ductile fracture. At temperatures higher than 0.4 T_m, creep becomes dominant deformation mechanism. In creep regime, Grade 91 steel deforms by transgranular and intergranular creep fracture. Transgranular creep fracture (TCF) is observed in high stress regime, while intergranular creep fracture (ICF) is observed at low stresses. Dominant failure mechanism in TCF is the microstructural degradation, nucleation, growth and coalescence of cavities. The fracture surface of transgranular creep is similar to that of low temperature ductile fracture (r-type cracking), but the rate-controlling deformation mechanism is the high temperature dislocation climb instead of low temperature dislocation glide in low temperature ductile fracture [9,46]. Transgranular creep fracture regime was identified by coupled Monkman–Grant equation (Eq. (6)) and modified BMD equation (Eq. (4)). After using these equations, the fractographic observation from various studies and tensile data were used to better delineate the domain of TCF. The shaded region indicates the transition between the TCF and ICF. ICF is characterized by w-type cracks, which nucleate and grow on grain boundaries. W-type cracks seen in the present study were mainly located away from necked region, the region which has not reached the minimum creep stage, but they were not observed in the necked region. ICF domain was calculated by Hull and Rimmer cavity growth rate equation [47] as mentioned in Li and Zinkle [46]

$$t_R = B \frac{kTa^3}{(D_{gb}\delta)\sigma\Omega}, \tag{12}$$

where B is the constant based on the spatial distribution of cavities, k the Boltzmann's constant, T the absolute temperature, a the mean cavity spacing, D_{gb} the grain boundary diffusivity, δ the grain boundary thickness, σ the applied stress, and Ω the atomic volume. The shaded region represents the variation in creep rupture life in the range of 10^4–10^5 h. To the best of our knowledge, Fig. 11 presents the first attempt at constructing the fracture mechanism map of Grade 91 steel. This could potentially lead to the development of fracture mechanism maps of other 9–12 wt% Cr F–M steels.

4. Conclusions

The creep deformation and fracture behavior of Grade 91 steel was studied in the temperature range of 600–700 °C and at stresses 35–350 MPa. Creep deformation mechanisms in higher and lower stress regimes were identified as dislocation climb and Nabarro–Herring creep, respectively. The fractography of creep ruptured specimens revealed dominant dimpled fracture surfaces (transgranular fracture mode), but some wedge type cavities were also observed. With the help of stress exponent and creep damage tolerance factor obtained, the dominant creep rupture mechanism was identified as microstructural degradation. The creep rupture data were analyzed in terms of Monkman–Grant relation, modified Monkman–Grant relation and Larson–Miller parameter. Fracture mechanism map of Grade 91 steel was constructed based on the available data.

Acknowledgment

References

[1] I. Charit, K.L. Murty, J. Mater. 62 (2010) 67–74.
[2] E. Barker, Mater. Sci. Eng. 84 (1986) 49–64.
[3] R.L. Klueh, Int. Mater. Rev. 50 (2005) 287–310.
[4] Y.Z. Shen, S.H. Kim, H.D. Cho, C.H. Han, W.S. Ryu, J. Nucl. Mater. 400 (2010) 64–68.
[5] M. Tanelke, F. Abe, K. Sawada, Nature 424 (2003) 294–296.
[6] K. Laha, K.S. Chandravathi, P. Parameswaran, K. Bhanu Sankara Rao, S.L. Mannan, Metall. Mater. Trans. A 38 (2007) 58–68.
[7] S. Sathyanarayanan, A. Moitra, K.G. Samuel, G. Sasikala, S.K. Ray, V. Singh, Mater. Sci. Eng. A 488 (2008) 519–528.
[8] K.L. Murty, I. Charit, J. Nucl. Mater. 383 (2008) 189–195.
[9] T. Shrestha, M. Basirat, I. Charit, G.P. Potirniche, K.K. Rink, J. Nucl. Mater. 423 (2012) 110–119.
[10] L. Kloc, V. Sklenicka, Mater. Sci. Eng. A 234–236 (1997) 962–965.
[11] P.J. Ennis, A. Zielinska-Lipiec, O. Wachter, A. Czyrska-Filemonowicz, Acta Mater. 45 (1997) 4901–4907.
[12] B.K. Choudhary, E.I. Samuel, J. Nucl. Mater. 412 (2011) 82–89.
[13] S. Spigarelli, E. Cerri, P. Bianchi, E. Evangelista, Mater. Sci. Technol. 15 (1999) 1433–1440.
[14] B. Ule, A. Nagode, Mater. Sci. Technol. 23 (2007) 1367–1374.
[15] M. Yurechko, C. Schroer, O. Wedemeyer, A. Skrypnik, J. Konys, J. Nucl. Mater. 419 (2011) 320–328.
[16] P. Anderson, T. Bellgard, F.L. Jones, Mater. Sci. Technol. 19 (2003) 207–213.
[17] C.G. Panait, A. Zielinska-Lipiec, T. Koziel, A. Czyrska-Filemonowicz, A.-F. Gourgues-Lorenzon, W. Bendick, Mater. Sci. Eng. A 527 (2010) 4062–4069.
[18] G.E. Dieter, Mechanical Metallurgy, 3rd ed., McGraw-Hill, Boston, MA, 1986.
[19] J.E. Bird, A.K. Mukherjee, J.E. Dorn, in: D.G. Brandon, A. Rosen (Eds.), Quantitative Relation Between Properties and Microstructure, Israel Universities Press, Jerusalem, Israel, 1969pp. 255–342.
[20] E. Cerri, E. Evangelista, S. Spigarelli, P. Bianchi, Mater. Sci. Eng. A 245 (1998) 285–292.
[21] K. Sawada, H. Kushima, M. Tabuchi, K. Kimura, Mater. Sci. Eng. A 528 (2011) 5511–5518.
[22] V. Sklenicka, K. Kucharova, M. Svoboda, L. Kloc, J. Bursik, A. Kroupa, Mater. Charact. 51 (2003) 35–48.
[23] J. Hald, Int. J. Pressure Vessels Piping 85 (2008) 30–37.
[24] Y. Qin, G. Gotz, W. Blum, Mater. Sci. Eng. A 341 (2003) 211–215.
[25] P.J. Ennis, A. Zielinska-Lipiec, A. Czyrska-Filemonowicz, in: A. Strang, J. Cawley, G.W. Greenwood (Eds.), Microstructural Stability of Creep Resistant Alloys for High Temperature Plant Applications, Institute of Materials, London, 1998p. 135.
[26] H. Riedel, Fracture at High Temperatures, Springer-Verlag, Berlin, Heidelberg, Germany, 1987, pp. 215–224.

[27] A.C.F. Cocks, M.F. Ashby, Prog. Mater. Sci. 27 (1982) 189–244.
[28] C.A. Hippsley, Acta Metall. 35 (1987) 2399–2416.
[29] B.K. Choudhary, K.B.S. Rao, S.L. Mannan, B.P. Kashyap, J. Nucl. Mater. 273 (1999) 315–325.
[30] F.C. Monkman, N.J. Grant, Proc. ASTM 56 (1956) 593–620.
[31] F.R.N. Nabarro, H.L. de Villiers, The Physics of Creep, Taylor & Francis, London, 1995, pp. 22–25.
[32] V.S. Srinivasan, B.K. Choudhary, M.D. Mathew, T. Jayakumar, Mater. High Temp. 29 (2012) 41–48.
[33] H.E. Evans, Mechanics of Creep Fracture, Elsevier Applied Science Publishers, New York, NY, 1984, pp. 18–22.
[34] F. Dobes, K. Milicka, Met. Sci. 10 (1976) 382–384.
[35] F.A. Leckie, D.R. Hayhurst, Acta Metall. 25 (1977) 1059–1070.
[36] M.F. Ashby, B.F. Dyson, in: S.R. Valluri, et al., (Eds.), Advances in Fracture Research, vol. 1, Pergamon Press, Oxford, 1984pp. 3–30.
[37] B.K. Choudhary, C. Phaniraj, B. Raj, Trans. Indian Inst. Met. 63 (2010) 675–680.

[38] B. Wilshire, H. Burt, Z. Metallkd. 96 (2005) 552–557.
[39] National Research Institute for Metals Creep Data Sheet, No. 43, Tokyo, 1996.
[40] M. Basirat, T. Shrestha, G.P. Potirniche, I. Charit, K. Rink, Int. J. Plast. 37 (2012) 95–107.
[41] B. Wilshire, P.J. Scharning, Int. Mater. Rev. 53 (2008) 91–104.
[42] F. Vivier, J. Besson, A.F. Gourgues, Y. Lejeail, Y. de Carlan, S. Dubiez, in: Le Goff, et al., (Eds.), Creep Behavior and Life Prediction of ASME Gr. 91 Steel Welded Joints for Nuclear Power Plants, Mines-Paris Tech, France, 2008pp. 1–2.
[43] E.M. Haney, F. Dalle, M. Sauzay, L. Vincent, I. Tournie, L. Allais, B. Fournier, Mater. Sci. Eng. A 510–511 (2009) 99–103.
[44] K. Kimura, H. Kushima, K. Sawada, Mater. Sci. Eng. A 510–511 (2009) 58–63.
[45] C. Gandhi, M.F. Ashby, Acta Metall. 27 (1979) 1565–1602.
[46] M. Li, S.J. Zinkle, J. Nucl. Mater. 361 (2007) 192–205.
[47] D. Hull, D.E. Rimmer, Philos. Mag. 4 (1959) 673–687.
[48] H.J. Frost, M.F. Ashby, Deformation Mechanism Maps, Pergamon Press, New York, NY, 1982, pp. 61–70.